Springer

KSME

Journal of Mechanical Science and Technology 33 (6) (2019) 2737~2746
www.springerlink.com/content/1738-494x(Print)/1976-3824(Online)
DOI 10.1007/s12206-019-0520-x

Investigation of wind tunnel wall effect and wing-fuselage interference regarding the prediction of wing aerodynamics and its influence on the horizontal tail †

Ngoc T. B. Hoang* and Binh V. Bui

School of Transportation Engineering, Hanoi University of Science and Technology, Dai Co Viet, Hai Ba Trung, Hanoi, Vietnam

(Manuscript Received December 23, 2018; Revised February 18, 2019; Accepted February 25, 2019)

Abstract

The calculation of aerodynamic characteristics of a wing is the basic problem for aerodynamic design of aircraft. Wing aerodynamics can be determined experimentally and numerically. The method of fixing the wing in the test chamber of wind tunnel is related to disturbance of flow through the wing. When the wing is entirely fixed in the test chamber, the disturbance is usually caused by the sting connecting the wing to the test chamber. The experiments in this paper fixed the wing by clamping to the wind tunnel wall at the wing symmetry surface (root section). With this wing fixation, it was possible to take advantage of the wingspan twice, but to obtain the 3D wing experiment results, it was necessary to evaluate the impact of the wind tunnel wall effect. As for aircrafts, the aerodynamic force of the aircraft's wing will have certain difference than that of the wing alone. The intersection region between the wind tunnel wall and wing root (for the experiment), as well as between the fuselage and wing root have complex interactions of boundary layers, in particular separation phenomena in the boundary layers. By solving the differential equation for viscous flows, it was possible to visualize the picture of streamlines and flow separations in this interference region and the aerodynamic characteristics of the wing. The singularity method was also used to compare results within its application range. The aerodynamic coefficients in the two cases with and without interference were analyzed. Complex interactions in the interference region could alter the predicted aerodynamic force calculated for the wing alone, which should be estimated. Very strong separations in the wing-fuselage interference region at large angles of attack turned into vortices at the rear impacting on the horizontal tail aerodynamics that is related to the balance problem of the aircraft.

Keywords: Wind tunnel wall effect; Wing-fuselage interference; Experiment; Numerical methods; Pressure distributions; Aerodynamic coefficients

1. Introduction

The wing is the main component that produces the lift for an aircraft and is thus studied carefully by various methods. Won et al. [1] studied the aerodynamic performance of basic airfoils using wind tunnel test (for measuring lift and drag forces). The wing was fixed in the wind tunnel by attaching two wing-tips to two walls of the test chamber. This type of wing fixation ensured high rigidity but prevented circular flows at the wing-tips and caused wind tunnel wall effect in both wing ends. Therefore, it is generally suitable for measuring aerodynamic characteristics of 2D case (profiles). Previous works [2-4] also had the same type of wing fixation (attaching two wing-tips to the two walls of the wind tunnel). In the Ref. [5], the authors used a sting to support the wing in the wind tunnel. With this installation, it was possible to study the aerodynamic characteristics of 3D wings (due to the existence of space outside the wing-tips). But experiments were performed only with wings whose size was not large in relation to the cross sectional area of the test chamber, and the sting caused disturbances of flows through the wing lower surface. Soltani et al. [6] and Hadidoolabi et al. [7] performed pressure measurements on solid wings by clamping the wing to the wind tunnel wall (at the wing root section). However, the use of the solid wing model only allowed the assessment of pressure measurements on one wing surface (upper or lower surface) during each measurement.

We performed pressure measurements on a half of hollow wings with the wing fixation by clamping it to the wind tunnel wall. With hollow wings, it was possible to simultaneously measure the pressure on the upper and lower surfaces of the wings. This fixation allowed the wingspan to be doubled, i.e., the wind tunnel wall was the symmetrical surface of the wing. However, to get 3D wing results, it was necessary to evaluate the wind tunnel effect on the aerodynamic characteristics of the wing. The experiment was conducted at different incidence angles, and the results showed that the wind tunnel wall effect was highly dependent on the incidence angle. The wing models used in our experiments were simultaneously also the wing models used for numerical calculations (solving the dif-

*Corresponding author. Tel.: +84 912313350
E-mail address: ngoc.hoangthibich@hust.edu.vn
† Recommended by Associate Editor Hyoung-Bum Kim

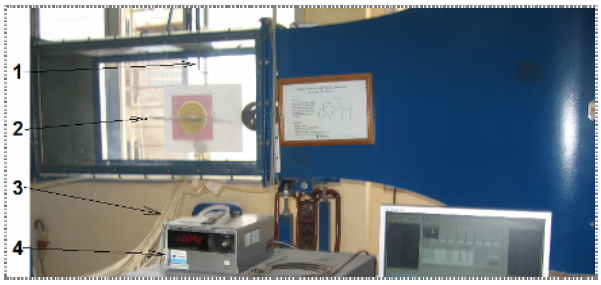

Fig. 1. Setup of the experiment (1. Pitot tube, 2. Hollow wing, 3. Flexible tubes, 4. Digital manometer).

ferential equations of viscous flows) in two cases with and without the presence of the wind tunnel wall.

In aircraft design, the aerodynamic forces are preliminary calculated for the wing alone. When the wing is attached to the fuselage (wing-fuselage system), there is a wing-fuselage interference, which changes aerodynamic forces compared with the forces calculated for the wing alone. This interaction effect depends on the angle of attack of the aircraft. Sobieczky's work [8] studied wing-fuselage interaction for optimization of aircraft configuration integration. Wolhart and Thomas [9] performed measurements of aerodynamic forces of wing alone (W) and wing-fuselage (WF) of aircraft models, which showed differences in aerodynamic force on the wing alone and wing-fuselage system. Our numerical calculations (using the Fluent software) were carried out for model aircrafts used in the experiments [9]. On one hand, these calculations compare numerical and experimental results. On the other hand, the calculations indicate the effects of physical phenomena on wing-fuselage interference region.

2. Methods determining flow interference effect

2.1 Experiments for measurement of pressures on the wing

Fig. 1 presents a test chamber of an open-return wind tunnel with cross section dimension (400 mm × 500 mm) in which a model wing was attached to the wind tunnel wall. The model wing was hollow in which flexible tubes (connecting gage holes with digital manometer) were arranged. Static pressures on the upper and lower surfaces of the wing were measured using a high-quality digital manometer with tolerance: ±0.15 % of full scale ±1digit = (±3±1) Pa. Flow velocities in the wind tunnel with Mach number M ≤ 0.15 were created using an exhaust axial fan [10]. The difference of pressures at the gage hole p and pressure obtained by the Pitot tube p_∞ was shown on the digital manometer and computer screens ($p - p_\infty$). For each pressure measurement value, the number of sampling times was set as 30000 to reduce the random error. The pressure coefficient C_p from experimental results was calculated as follows:

$$C_p = \frac{p - p_\infty}{0.5\rho V_\infty^2}, \quad (1)$$

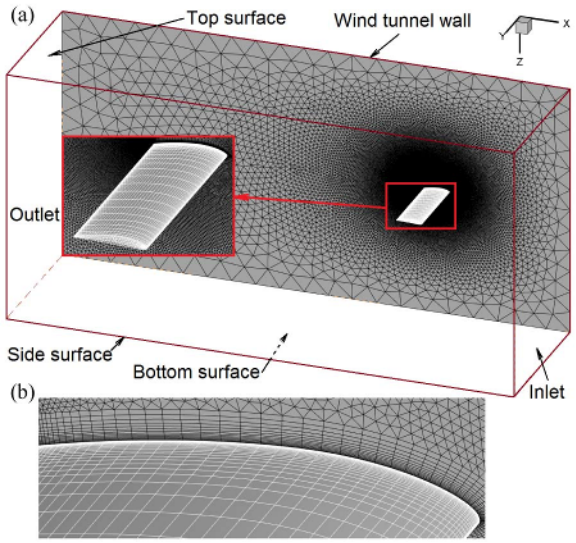

Fig. 2. (a) Mesh on the wind tunnel wall surface and face mesh over the wing; (b) generated boundary layer mesh and wing face mesh at the interference region near the wing root.

where ρ is the air density (at T = 30 °C, ρ = 1.14 kg/m^3), and V_∞ is the velocity in the wind tunnel (M_∞ = 0.1).

2.2 Numerical methods for calculating wing pressures

The pressure distribution on the wing was calculated using the Fluent software for viscous flows. The wing models used in numerical simulation were the wing models in experiment. Fig. 2(a) describes the meshing boundaries for a wing. The inlet, top and bottom surfaces were 6C (C was the mean chord of the wing) far away from the wing leading edge. The side surface was 2b (b was a half of wingspan) far away from the wing root. The outlet surface was 30C far away from the wing trailing edge.

Fig. 2(a) also presents the mesh on the wind tunnel wall (or wing symmetry surface) and the face mesh over the wing. The spacing of the face mesh over the wing-tip was small enough due to the wing-tip vortex effect. Where the wind tunnel wall effect was not accounted for, the wall was treated as a symmetry surface at which the symmetry condition was imposed and the spacing of the face mesh near the wing root was larger than that near the wing-tip [11]. However, where the wind tunnel wall was taken into consideration, to determine flow parameters in the interference region of flows around the wing and the wall, the face mesh near the wing root had very high resolution as shown in Fig. 2(b). The pressure distribution on the 3D wing was also determined by the singularity method (source - doublet) considering the wing thickness [12, 13]. This method can calculate pressures distributed on the wing with high accuracy as compared with experimental results and numerical results solving the differential equations (using the Fluent software). However, the singularity method is based on the assumption of non-viscous flow and the grid used in this method is divided on the wing surface, so the singularity

method is not suitable for determining the wing-tip effect and the wing downwash [11]. In this study, the wind tunnel wall effect as well as the wing-fuselage interference is related to the boundary layer separation, so using the singularity method is not effective. In this case, solving the differential equations for viscous flows by applying Fluent software was appropriate. Numerical results calculated from Fluent software were compared with experimental results and numerical results using the singularity method (with cases of ignoring flow separations).

2.3 Experimental results of pressure coefficients on the wing compared with numerical results

The wing model used in the experiment was rectangular with the profile NACA 4412 and had a chord length c = 100 mm and a half of the wingspan b = 300 mm. To avoid disturbance of the flow around the wing, all flexible tubes connecting the gage holes with the digital manometer were arranged in the wing (Fig. 1). There were 220 holes with 0.4 mm diameter (in 11 rows) drilled on the upper and lower surfaces of the wing (Fig. 5). The actual total was 12 rows of holes, but there was a row of 20 holes being in the wind tunnel wall (Fig. 5). The distance from the wing tip to the wall was 100 mm (equal to C). (This distance was enough to create a space for the circular flow from the wing lower to the upper sides at the wing tip).

Fig. 3 shows experimental results of pressure coefficients on wing Secs. 3, 5, 7, 9 compared to the numerical results using the singularity method and using the Fluent software (with the incidence angle $\alpha = 14^o$). The experimental and numerical results have considerably small differences. The distribution of the pressure coefficients on two sections near the wind tunnel wall (Secs. 1 and 2) is analyzed in Sec. 3.1 (in Fig. 7(a)).

Experimental results and numerical results calculated using the two numerical methods at $\alpha = 4^o$ are presented in Fig. 4 (2D representation on three Secs. 4, 6 and 8 and 3D representation on eleven sections). The experimental and numerical results were similar. With $\alpha = 4^o$, the pressure coefficient distribution on two sections near the wind tunnel wall (Secs. 1 and 2) was not different (see 2D representation of pressure coefficients on Secs. 1 and 2 in Fig. 6(b) in Sec. 3.1). This shows that the wind tunnel wall did not affect Sec. 1 located 40 mm away from the wall (see Fig. 5) with $\alpha = 4^o$. Analyses and evaluations of the wind tunnel wall effect on the aerodynamic characteristics of the wing are presented in Sec. 3.

3. Wind tunnel wall effect on the wing aerodynamics

3.1 Experimental results for wing sections near the wall

A photograph of the wing model in the experiment is shown in Fig. 5. The row of 20 holes closest to the wind tunnel wall (Sec. 1) was 40 mm from the wall, and the row of holes (Sec. 2) was 80 mm from the wall. With $\alpha = -4^o$ and $\alpha = 4^o$, the

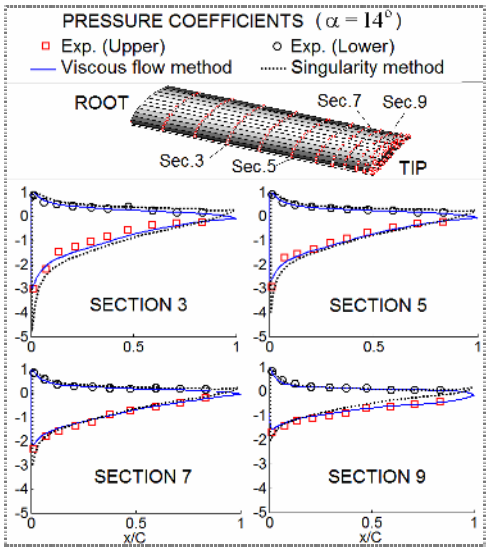

Fig. 3. Pressure coefficients on four Secs. 3, 5, 7 and 9 ($\alpha = 14^o$).

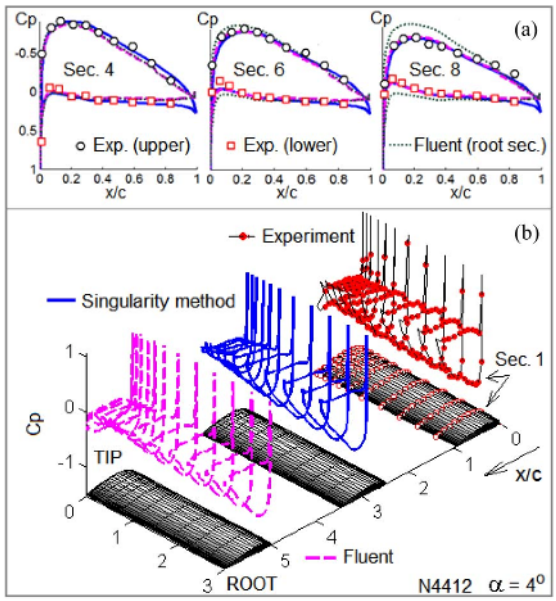

Fig. 4. (a) Pressure coefficients on three Secs. 4, 6 and 8; (b) 3D representation of pressure coefficients on 11 sections ($\alpha = 4^o$).

pressure coefficient distributions on Secs. 1 and 2 were almost the same as shown in Fig. 6, i.e., they were not subjected to the wind tunnel wall effect.

With $\alpha = 14^o$ and $\alpha = 18^o$, the pressure distributions on Secs. 1 and 2 were much different on the upper sides as shown in Fig. 7. Thus, at these incidence angles, the effect of the wind tunnel wall on the pressure distribution at Secs. 1 and 2 (on the upper sides) was significant. This phenomenon is illustrated and analyzed more specifically with simulation results presented in Sec. 3.2.

Graphical representations of the true mean value and error bar (based on the standard deviation (SD)) of pressure measurement at 10 holes on the lower side of Sec. 1 (with $\alpha = 14^o$)

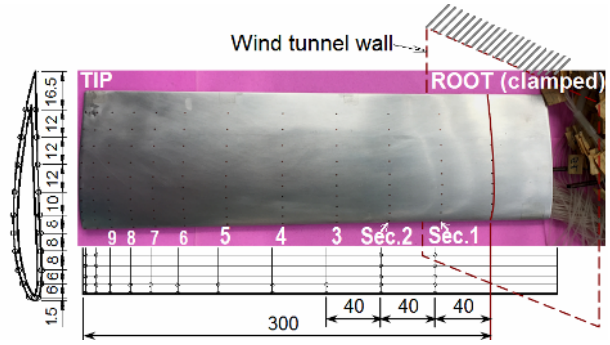

Fig. 5. Hollow wing and location of pressure gauge holes at Secs. 1 and 2 (40 mm and 80 mm far away from the wind tunnel wall).

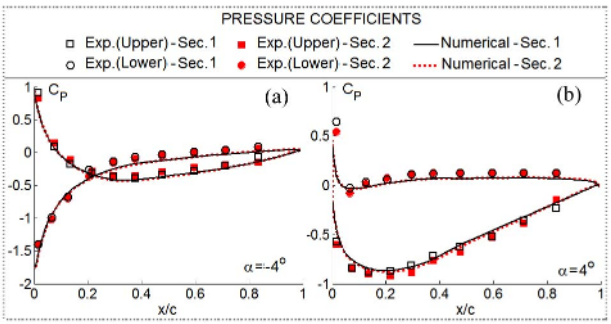

Fig. 6. Pressure coefficients on the sections near the wing root (Secs. 1 and 2): (a) $\alpha = -4^o$; (b) $\alpha = 4^o$.

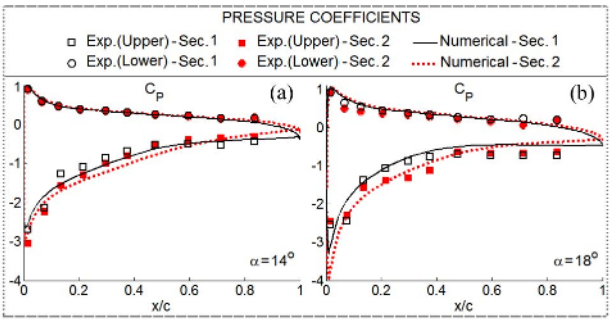

Fig. 7. Pressure coefficients on the sections near the wing root (Secs. 1 and 2): (a) $\alpha = 14^o$; (b) $\alpha = 18^o$.

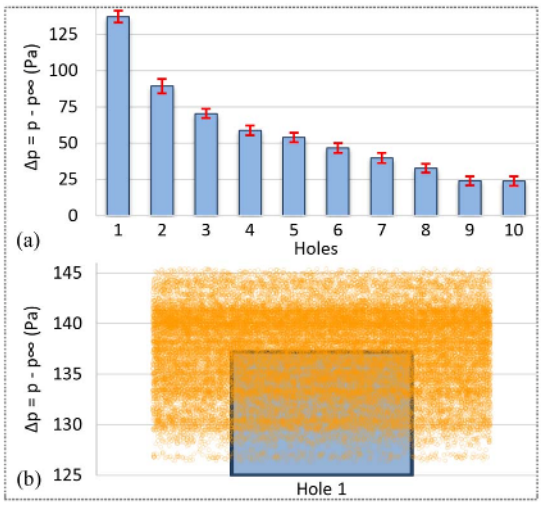

Fig. 8. (a) True mean values and error bars (of 30000 sampling times) of pressure measurement at 10 holes on the lower side of Sec. 1 ($\alpha = 14^o$); (b) dispersion of 30000 data points of measurement pressure at hole 1.

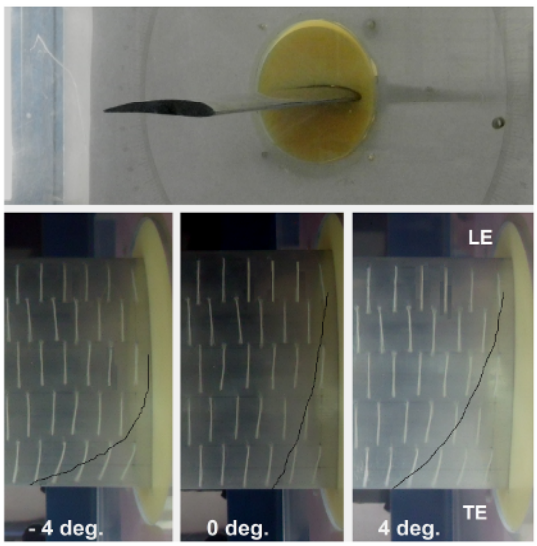

Fig. 9. Flow visualization on upper surface at incidence angles $\alpha = -4^o$, 0^o, 4^o (profile NACA 4412).

are presented in Fig. 8(a). The dispersion of pressure measurement points of 30000 sampling times at hole 1 is indicated in Fig. 8(b).

The formula for the sample standard deviation σ is:

$$\sigma = \sqrt{\frac{\sum_{i=1}^{n}\left(\Delta p_i - \Delta\overline{p}\right)^2}{n-1}}, \quad (2)$$

where Δp_i refers to the individual data points, $\Delta\overline{p}$ is the mean and n is the number of sampling times (n = 30000). Standard deviation σ is the typical difference between the data points Δp_i and their mean $\Delta\overline{p}$. About two-thirds of the data points Δp_i will lie within the region of $\Delta\overline{p} \pm \sigma$ (the length of red bar is 2σ).

Fig. 9 shows the photographs of flow visualization with silk threads glued to the wing upper surface at incidence angles $\alpha = -4^o$, 0^o and 4^o. The wing was clamped (root section) into a wind tunnel wall (each thread row was 10 mm apart) [14, 15]. The wing used in this experiment was rectangular and had a half of the wingspan b = 300 mm, and the chord length C = 100 mm. The open-return wind tunnel had the test section dimension of (400 mm × 500 mm) [16]. The experimental results in Fig. 9 show that the wind tunnel effect pushed the silk threads away from the wall and made them no longer parallel to the wall. The affected area had a curved triangular shape. The affected distance at the trailing edge (TE) was 40 mm and 30 mm with $\alpha = 4^o$ and $\alpha = 0^o$, respectively. At $\alpha = -4^o$, only the

threads near the trailing edge were tilted. With the wing model in this experiment (chord length C = 100 mm) and the incidence angles mentioned above, the distance from the test chamber wall of 40 mm was acceptable to bypass the effect of wind tunnel wall (this means that the pressure measured at distances equal to and greater than 40 mm against the wind tunnel wall was considered to be the actual pressure on the wing). This flow visualization experiment also yielded the same results as the pressure measurements on two adjacent sections near the wall (Secs. 1 and 2) with $\alpha = -4^o$ and $\alpha = 4^o$ as shown in Figs. 6(a) and (b).

3.2 Simulation results

Fig. 10 presents the simulation results of the flow through the wing with $\alpha = 4^o$ in two cases without and with the wind tunnel wall. Consider surface A being 5 mm (5 % C) away from the wind tunnel wall. Fig. 10(a) shows streamlines on surface A in the case without the wind tunnel wall (the position of the wall was the symmetry surface of the wing) and Fig. 10(b) shows streamlines on surface A with the presence of the wind tunnel wall (case of the experiment). As compared with the results shown in Fig. 10(a), the results of streamlines in Fig. 10(b) had strong boundary layer separations which became vortices behind the wing. The distribution of the lift coefficients on a half wingspan in Fig. 10(c) shows the difference of the lift coefficients in two cases with and without the wind tunnel wall effect. The interference between the flow over the wing (near the wing root) and the flow on the wind tunnel wall caused separations and reduced the lift coefficient in the region near the wing root. The difference in the pressure coefficient distribution on Sec. A in the two cases with and without the wind tunnel walls is shown in Fig. 10(d).

With $\alpha = 14°$, the flow interference in the region near the wing root caused very strong separations as presented in Fig. 11(b) showing streamlines on the surface A. The lift coefficients on a half of wingspan were significantly reduced near the wing root due to the wind tunnel wall effect (compared with the case without the wall) as shown in Fig. 11(c). The pressure distribution on Sec. A in Fig. 11(d) shows a large difference in the two cases with and without the wind tunnel wall effect.

The distribution of lift coefficients in Figs. 10(c) and 11(c) shows the difference between the results with and without the wind tunnel wall effect at sections near the wall. The numerical results presented in Table 1 allows to evaluate the deviation of lift coefficients caused by the wind tunnel wall effect at three Secs. 1-3 with two cases $\alpha = 4°$ and $\alpha = 14°$ (y was the distance from the wall to the pressure measuring hole). With $\alpha = 4°$, the lift coefficient deviations (at 3 Secs. 1-3) of the two cases with and without the wall were equal to and less than 5 %. Therefore, the effect of the wind tunnel wall was negligible for the measurement pressure at the holes of the three Secs. 1-3. With $\alpha = 14°$, the lift coefficient deviation at Sec. 1 was 13 % (i.e., the wall effect was significant, which was similar to

Table 1. Lift coefficients without the wall ($C_{L(sym.)}$) and with the wall ($C_{L(wall)}$) at three sections near the wing root.

Secs.	y (mm)	$\alpha = 4^o$			$\alpha = 14^o$		
		$C_{L(sym)}$	$C_{L(wall)}$	Δ (%)	$C_{L(sym)}$	$C_{L(wall)}$	Δ (%)
Sec. 1	40	0.600	0.570	5.0 %	1.261	1.097	13 %
Sec. 2	80	0.594	0.579	2.5 %	1.254	1.194	4.8 %
Sec. 3	120	0.582	0.573	1.5 %	1.238	1.217	1.8 %

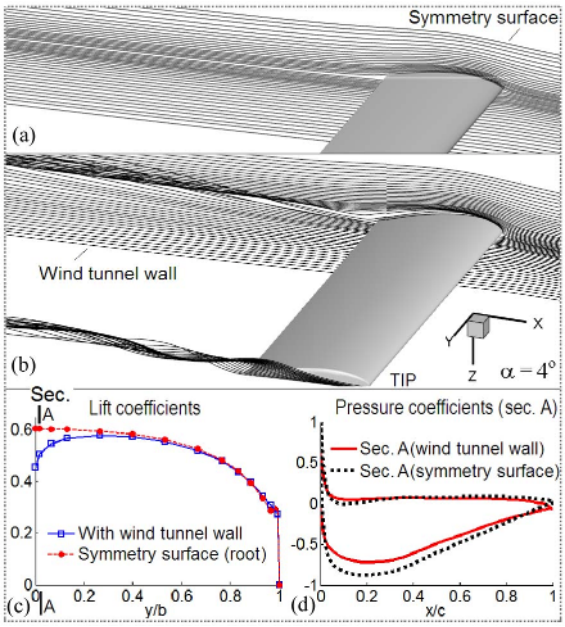

Fig. 10. Simulation rerults, $\alpha = 4^o$: (a) Streamlines through A (without the wall); (b) streamlines through A (with the wall); (c) lift coefficients on wingspan-half; (d) pressure coefficients on Sec. A.

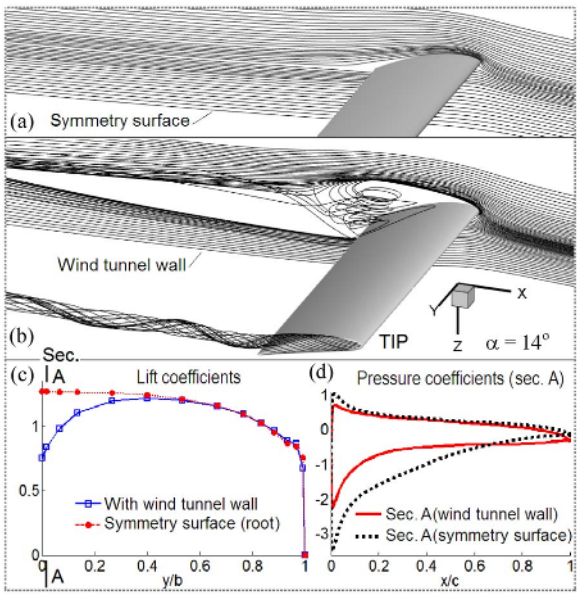

Fig. 11. Simulation rerults, $\alpha = 14^o$: (a) Streamlines through A (without the wall); (b) streamlines through A (with the wall); (c) lift coefficients on wingspan-half; (d) pressure coefficients on Sec. A.

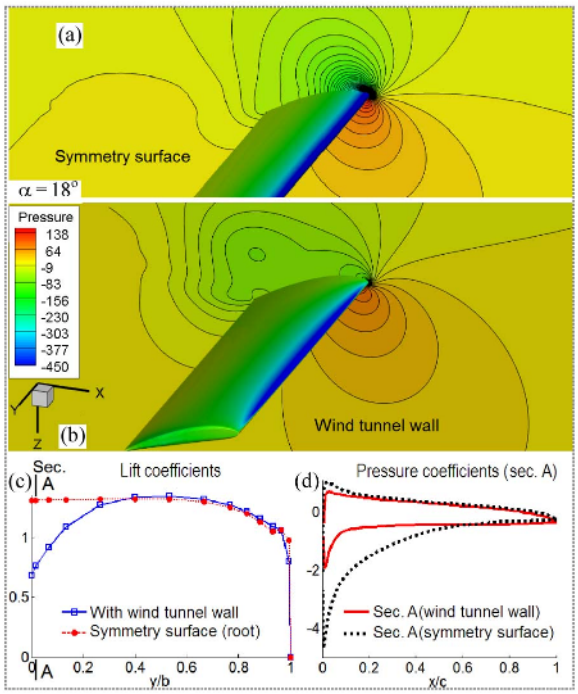

Fig. 12. Simulation results, α = 18°: (a) Pressure contours on A (without the wall); (b) pressure contours on A (with the wall); (c) lift coefficients on wingspan-half; (d) pressure coefficients on Sec. A.

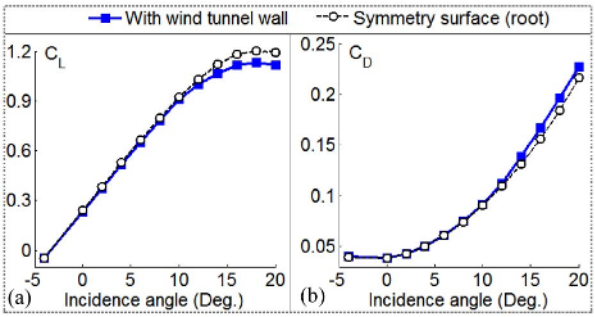

Fig. 13. Aerodynamic force coefficients for two cases with and without the wind tunnel wall: (a) Lift coefficients; (b) drag coefficients.

commenting on the result in Fig. 7(a)). From distance of y = 80 mm and larger (Secs. 2 and 3), the deviation was less than 5 %.

The difference in pressure contours on Sec. A near the wing root in two cases with and without the wind tunnel wall with α = 18° is shown in Figs. 12(a) and (b). The lift coefficient near the wing root decreased sharply in the case with the wall effect (Fig. 12(c)). The pressure coefficient in Sec. A as shown in Fig. 12(d) was very different for the two cases with and without the wind tunnel wall effect. Fig. 13 presents the lift and drag coefficients of the wings with respect to the incidence angle in the two cases with and without the wind tunnel wall. The results in Fig. 13 indicate that the wall effect was severe with large incidence angles.

With the model wings used in the experiment and numerical simulations above, the wind tunnel wall effect was significant with α > 10°. The distance of 40 mm (0.4C) between Sec. 1 (row of holes measuring pressures) and the wind tunnel wall was satisfying to ignore the wall effect with α < 10°. This statement only applies to the determination of the lift coefficient and drag coefficient. However, the difference in the pressure distributions on the wing in the two cases with and without the wall effect was related to the distributions of the load on the wing. The relation between the load distribution on the wing and the wing aero-elasticity problem or the balance of the aircraft is discussed in more detail in Sec. 4.

Table 2. The fuselage coordinates of the model in the experiment.

Station x (in)	Radius r (in)	Station x (in)	Radius r (in)	Station x (in)	Radius r (in)
0	0	16	2.96	32	2.6
2	0.64	18	3	34	2.47
4	1.2	20	2.99	36	2.33
6	1.68	22	2.97	38	2.18
8	2.09	24	2.93	40	2.01
10	2.42	26	2.87	42	1.82
12	2.67	28	2.79	44	1.61
14	2.85	30	2.7	45	1.5

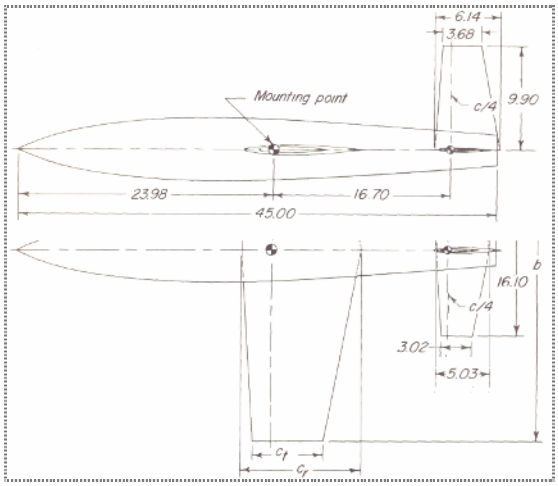

Fig. 14. Principal dimensions of the model in the experiment [9].

4. Wing-fuselage interference effect

4.1 Aircraft model in experiment

Wolhart and Thomas [9] performed experiments to measure aerodynamic forces of aircraft models in a wind tunnel to determine the static stability characteristics. By using the Fluent software, we performed simulations for a model in this experiment to determine the aerodynamic coefficients and compared them with the experimental results. The principal dimensions of the model are shown in Fig. 14. The main wing (and tail) had the profile NACA 65A008, the root chord C_r = 9.18 in, the tip chord C_t = 5.5 in, the span b = 44.1 in. Fuselage coordinates of the model are given in Table 2.

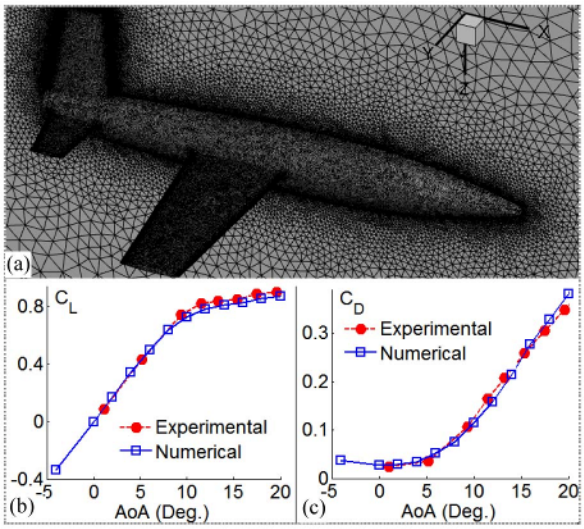

Fig. 15. (a) Mesh on symmetry surface of the model (in the experiment); (b) lift coefficients; (c) drag coefficients.

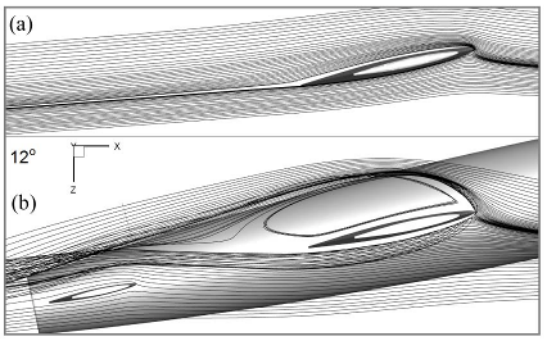

Fig. 16. Streamlines on wing root section with AoA = 12°: (a) Wing alone; (b) wing-fuselage combination.

Fig. 15 presents the comparisons of the numerical results and the experimental results for the model in the experiment [9]. With angles of attack AoA < 20°, both the lift coefficient (Fig. 15(b)) and the drag coefficient (Fig. 15(c)) show a similarity between the numerical results and the experimental results (deviation was less than 3 %). Lift coefficients of the wing alone (W) and wing-fuselage combination (WF) are presented in Sec. 4.2.

4.2 Wing-fuselage interference effect on the wing

Fig. 16 shows the streamlines through the wing root section in two cases of the wing alone (Fig. 16(a)) and wing-fuselage combination (Fig. 16(b)) with AoA = 12° (wing setting angle was zero). In the case of the wing alone, the flow separations occurred on the upper side of the wing root section and the streamlines were still smooth. In the case of the wing-fuselage combination, the separations occurred on both the upper and lower sides of the wing. Particularly, on the upper side, very large separations covered the entire wing and extended to the rear of the wing. The streamlines through the model at AoA = 4° and AoA = 8° are shown in Fig. 17. With AoA = 8°, in the wing-fuselage interference region there were large separations which were followed by a vortex strip (Fig. 17(b)).

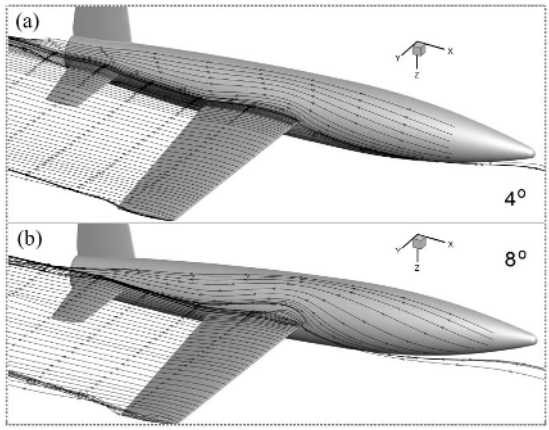

Fig. 17. Simulation results on streamlines through the model: (a) Angle of attack AoA = 4°; (b) angle of attack AoA = 8°.

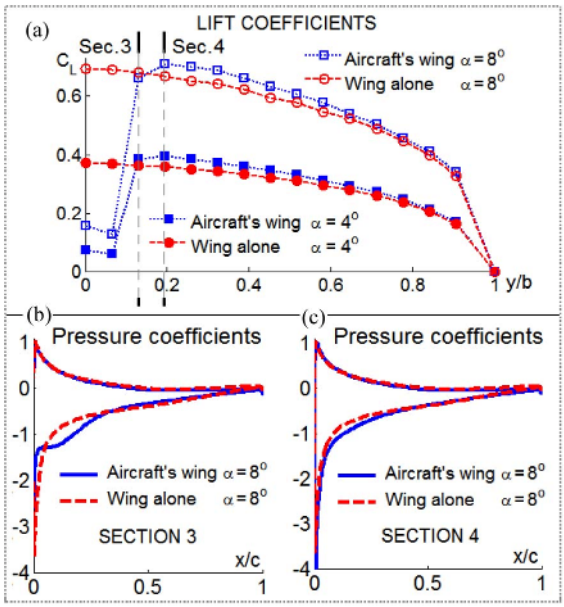

Fig. 18. (a) Lift coefficients on a half of the wing (AoA = 4°, AoA = 8°); (b) pressure coefficients on section 3 (AoA = 8°); (c) pressure coefficients on section 4 (AoA = 8°).

The lift coefficients on a half of the wing for the wing alone and the model's wing (with AoA = 4° and AoA = 8°) are shown in Fig. 18(a). The differences of lift coefficients of the two cases depended on the position of the wing relative to the fuselage [17-19]. In this study, it was limited to the case of a given model (in experiment).

The differences in the lift distribution on the wingspan as well as the pressure distribution on wing sections (Fig. 18(c)) for the wing alone and wing-fuselage combination were related to the load-bearing capacity of the wing structure. This is further analyzed by considering the total aerodynamic force of the wing in Fig. 19.

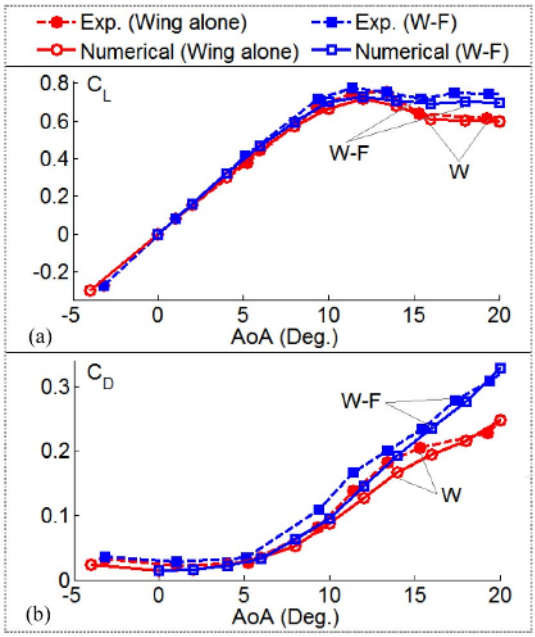

Fig. 19. Aerodynamic coefficients of the wing alone and wing-fuselage combination: (a) Lift coefficients; (b) drag coefficients.

Fig. 19 presents the numerical results compared with the experimental results [9] of the lift and drag coefficients with respect to the angle of attack for the wing alone and the wing-fuselage combination of the model. At angles of attack AoA < 8^o, the aerodynamic coefficients of the wing alone and the wing-fuselage combination were not much different (the presence of the fuselage slightly increased the drag coefficient and caused a very minor change the lift coefficient). With AoA ≥ 12^o, the separations were very strong in the wing-fuselage interference region, which increased the drag of the wing-fuselage combination compared with the one of the wing alone. With AoA = $12^o \div 20^o$, the wing-fuselage interference effect also caused significant increases in the lift coefficient compared to those of the wing alone.

However, even in the range of AoA < 8^o, the average value (by integration) of the lift coefficient only varied slightly, but the difference of lift coefficient distribution on the wingspan, and the difference of the pressure distribution on sections were related to the load distribution on the wingspan. In practice, the actual aerodynamic force of the wing under elastic deformation depends on the distribution of the local load on the wing [12].

4.3 Wing-fuselage interference effect on the horizontal tail

Fig. 20 shows the numerical results of the pressure distributions on the horizontal tail and streamlines through the wing root surface in two cases of the complete model (wing-fuselage-vertical-horizontal tail, WFVH) and the wing-tail combination (WVH) with AoA = 12^o. The streamlines were separated very strongly in the wing-fuselage interference region as shown in Fig. 20(a) (see Fig. 16). The pressure distributions on the horizontal tail differed significantly in the two cases with and without the wing-fuselage interference. The graphs showing aerodynamic coefficients of the model's components in Fig. 21 indicate that the lift coefficient of the vertical tail (V) was zero (the drag coefficient was nearly zero).

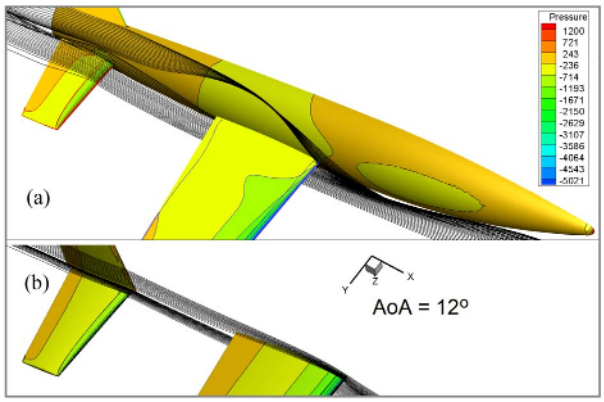

Fig. 20. Streamlines through the wing root surface and pressure distributions on the horizontal tail (with AoA = 12^o): (a) Complete model; (b) wing-tail combination.

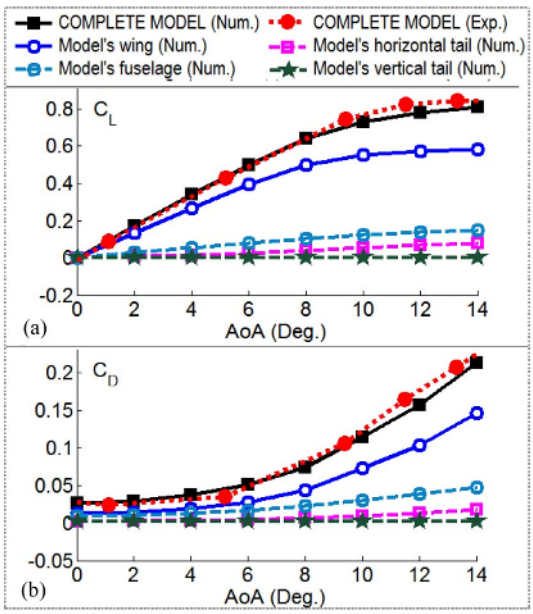

Fig. 21. Aerodynamic coefficients of the complete model and its components: (a) Lift coefficients; (b) drag coefficients.

The horizontal tail lift has a great bearing on the balance and stability problems of the aircraft. The results in Fig. 21 show that the lift and drag coefficients of the horizontal tail were much smaller than those of the main wing. However, the lift of the horizontal tail was the main component producing pitching moment of the aircraft (due to large arm from the tail aerodynamic center to the gravity center of the aircraft). Thus, a small change in the lift of the horizontal tail also affected the balance and stability of the aircraft. Experimental work [9] did not measure the aerodynamic force of the horizontal tail alone (H), but only measured the aerodynamic force of the vertical-

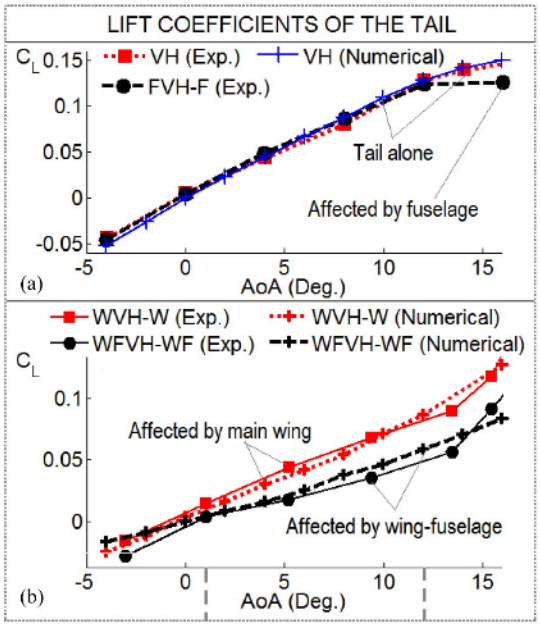

Fig. 22. Lift coefficients of the horizontal tail (H is equivalent to VH): (a) For tail alone and tail affected by fuselage; (b) for tail affected by wing and wing-fuselage combination.

horizontal tail combination (always tested as a unit VH). Therefore, a numerical computation was also performed with the vertical-horizontal tail combination (VH) to compare with the experimental results (as shown Fig. 22(a)). Simulation results for the complete model have resulted in the aerodynamic coefficients of each component as shown in Fig. 21. The numerical results (shown in Fig. 21(a)) indicate that the lift coefficient of the vertical tail (affected by the wing, fuselage and horizontal tail) was zero. Thus, in this case, the lift coefficient of the vertical-horizontal tail combination (VH) was equivalent to the lift coefficient of the horizontal tail (H).

Returning to the analysis of the effect of separations in the wing-fuselage interference region to the lift coefficient of the horizontal tail. The graphs in Fig. 22(a) show that, with angles of attack -4° to 12°, the interaction between the fuselage and tail did not alter the lift coefficient on the horizontal tail (when comparing the lift coefficient of the tail alone (VH) with the lift coefficient of the fuselage-tail combination minus fuselage alone (FVH – F)).

The graphs in Fig. 22(b) show the effect of separations in the wing-fuselage interference region on the lift coefficient of the horizontal tail. The lift coefficient of the horizontal tail influenced by the main wing (WVH – W) was significantly different from that influenced by the wing-fuselage combination (WFVH – WF). The deviation was up to nearly 40 % with angles of attack 8° to 12°. This difference was highly related to the balance and stability of the aircraft.

5. Conclusions

Experimental and numerical studies for a wing fixed in a test chamber by clamping at the wing symmetry surface (root section) showed that the wind tunnel wall effect was significant. This effect increased with the increase of the incidence angle. To determine aerodynamic forces of 3D wings in experiment, it is necessary to evaluate the wind tunnel wall effect when using the wing fixation method in the wall by clamping. This fixation method has the advantage of doubling the wingspan. In addition, if the wing is machined hollow, it is very convenient to take the pressure gauge tubes from the inside of the wing to the outside through the wing root clamped in the wind tunnel wall. This avoids the flow disturbance caused by the pressure gauge tubes.

In the design of aircraft, the aerodynamic shape of the wing is calculated to ensure optimum aerodynamic quality. However, there may be significant changes in aerodynamic forces when considering the wing-fuselage interference effect. The above studies show that, at great angles of attack, very strong separations occurred in the wing-fuselage interference region, so both the lift and drag coefficients of the wing-fuselage system were much different than that of the wing alone. This means that the aerodynamic force of the aircraft's wing was significantly different from that predicted for the wing alone.

According to the studied results, with small angles of attack, the lift and drag coefficients of the two cases of the wing alone and wing-fuselage system might not be very different. However, the pressure distribution at the interference region was somewhat different in these two cases. This difference may be important from the perspective of local loading on the wing. Therefore, experimental and numerical determinations of the pressure distribution on the wing (as was done in this work) are significant. This pressure distribution gives an understanding of the load distribution law as the input parameter for the strength problem and the aeroelasticity problem of the wing. In addition, strong separations in the wing-fuselage interference region are turned into vortices that affect the horizontal tail, which is related to the balance and stability problems of the aircraft.

References

[1] Y. S. Won, B. A. Haider, C. H. Sohn and Y. M. Koo, Aerodynamic performance evaluation of basic airfoils for an agricultural unmanned helicopter using wind tunnel test and CFD simulation, *J. of Mechanical Science and Technology*, 31 (12) (2017) 5829-5838.

[2] M. Masdari, M. Jahanmiri, M. R. Soltani, A. Tabrizian and M. Gorji, Experimental investigation of a supercritical airfoil boundary layer in pitching motion, *J. of Mechanical Science and Technology,* 31 (1) (2017) 189-196.

[3] J. Piquee and C. Breitsamter, Numerical and experimental investigations of an elasto-flexible membrane wing at a Reynolds number of 280000, *Aerospace*, 4 (2017) 39-55.

[4] G. Fillola, G. Carrier and J-B. Dor, Experimental study and numerical simulation of flow around wing control surface, *ICAS-Secretariat - 25th Congress of the International Coun-*

cil of the Aeronautical Sciences (2006).

[5] E. Tangermann, M. Klein, S. L. Herbst, R. Hain and C. J. Kahler, Numerical and experimental investigation of the flow around a three-dimensional SD7003 wing, *10th International Symposium on Turbulence and Shear Flow Phenomena (TSFP10),* Chicago, USA (2017).

[6] M. R. Soltani, M. Masdari and M. R. Tirandaz, Effect of an end plate on surface pressure distributions of two swept wings, *Chinese J. of Aeronautics*, 30 (5) (2017) 1631-1643.

[7] M. Hadidoolabi and H. Ansarian, Supersonic flow over a pitching delta wing using surface pressure measurements and numerical simulations, *Chinese J. of Aeronautics*, 31 (1) (2017) 65-78.

[8] H. Sobieczky, Configuration test cases for aircraft wing root design and optimization, *International Symposium on Inverse Problems in Engineering Mechanics,* Nagano, Japan (1998) 371-380.

[9] W. D. Wolhart and D. F. Thomas Jr, *Static Longitudinal and Lateral Stability Characteristics at Low Speed of Unswept-Midwing Models Having Wings with an Aspect Ratio of 2, 4, or 6*, National Advisory Committee for Aeronautics, Langley Aeronautical Lab, Washington, USA (1956).

[10] M. H. Nguyen and T. B. N. Hoang, Experimental study of laminar separation phenomenon combining with numerical calculations, *Vietnam J. of Mechanics*, 33 (2) (2011) 95-104.

[11] T. B. N. Hoang and V. B. Bui, Experimental and numerical studies of wing-tip effect and wing downwash affecting the horizontal tail, *J. of Mechanical Science and Technology*, 33 (2) (2019) 649-659.

[12] T. B. N. Hoang, Computational investigation of the variation in wing aerodynamic load under the effect of aeroelastic deformations, *J. of Mechanical Science and Technology*, 32 (10) (2018) 4665-4673.

[13] J. Katz and A. Plotkin, *Low Speed Aerodynamics*, 2nd Ed., Cambridge University Press, New York, USA (2001).

[14] S. Ristic, Flow visualisation techniques in wind tunnels Part I – Non optical methods, *Scientific Technical Review*, LVII No. 1 (2007).

[15] D. Filipiak, R. Szczepaniak, T. zahorski, R. Babel, S. Stabryn and W. Stryczniewicz, Flow visualization over an airfoil with flight control surfaces in a water tunnel, *Transactions of the Institute of Aviation*, 1 (246) (2017) 63-78.

[16] H. S. Nguyen, T. B. N. Hoang, V. P. Dinh and M. H. Nguyen, Experiments and numerical calculation to determine aerodynamic characteristics of flows around 3D wings, *Vietnam J. of Mechanics,* 36 (2) (2014) 133-143.

[17] R. Berger and L. M. M. Boermans, Aerodynamic design of the wing-fuselage junction for the high-performance sailplane Mu-31, *Technical Soaring*, 28 (3) (2004) 13-23.

[18] N. Deng, Q. Qu and R. K. Agarwal, Numerical study of the aerodynamics of DLR-F6 wing-body in unbounded flow field and in ground effect, *55th AIAA Aerospace Sciences Meeting,* Texas (2017).

[19] H. Schlichting and E. A. Truckenbrodt, *Aerodynamics of the Airplane*, McGraw-Hill, USA (1979).

Hoang Thi Bich Ngoc, who is an Associate Professor at the School of Transportation Engineering, HUST, Vietnam, acquired her M.A. and Ph.D. in France. Fields of interest include aerodynamics, aeroelasticity, flight mechanics, turbo-machines, and computational calculations.

Bui Vinh Binh received his B.E. (2012) from the Excellent Engineer Training Program (PFIEV) and his M.A. (2014) at HUST. He is currently a Ph.D. candidate at HUST. Fields of interest include aerodynamics and airplane stability.